

Explicit quantum surrogates for quantum kernel models

Akimoto Nakayama,^{1,2,*} Hayata Morisaki,^{1,†} Kosuke Mitarai,^{1,2,‡} Hiroshi Ueda,^{2,3,§} and Keisuke Fujii^{1,2,4,¶}

¹Graduate School of Engineering Science, Osaka University,
1-3 Machikaneyama, Toyonaka, Osaka 560-8531, Japan

²Center for Quantum Information and Quantum Biology,
Osaka University, 1-2 Machikaneyama, Toyonaka, Osaka 560-0043, Japan

³Computational Materials Science Research Team, RIKEN Center for Computational Science (R-CCS), Kobe, Hyogo 650-0047, Japan

⁴RIKEN Center for Quantum Computing (RQC), Hirosawa 2-1, Wako, Saitama 351-0198, Japan

(Dated: August 7, 2024)

Quantum machine learning (QML) leverages quantum states for data encoding, with key approaches being explicit models that use parameterized quantum circuits and implicit models that use quantum kernels. Implicit models often have lower training errors but face issues such as overfitting and high prediction costs, while explicit models can struggle with complex training and barren plateaus. We propose a quantum-classical hybrid algorithm to create an explicit quantum surrogate (EQS) for trained implicit models. This involves diagonalizing an observable from the implicit model and constructing a corresponding quantum circuit using an extended automatic quantum circuit encoding (AQCE) algorithm. The EQS framework reduces prediction costs, mitigates barren plateau issues, and combines the strengths of both QML approaches.

Quantum machine learning has attracted significant interest in recent years as a potential application of quantum computers [1, 2]. Particularly interesting approaches to quantum machine learning are those based on the idea of a quantum feature map, which aims to gain performance improvement over classical techniques via the use of quantum states for storing features of given data. [3–9]. Models using quantum features can be broadly classified into two categories: the explicit quantum models based on parameterized quantum circuits [6–8] such as quantum circuit learning [9], and the implicit models based on quantum kernels [3–5]. The former makes predictions about an input from the output of a single quantum circuit, which first embeds the input into a quantum state and then applies a parameterized quantum circuit to select important features stored in the state. The model is therefore *explicitly* specified via the description of the circuit used for prediction. In contrast, the latter does so by calculating inner products of quantum features, that is, quantum kernel functions, among the data points and assessing them on a classical machine. It is therefore *implicit* in the sense that the quantum circuit itself does not describe the model. It has been demonstrated that both quantum models are capable of achieving good learning performance in benchmark tasks, as seen in numerical simulations [4, 10–15] and experiments using real quantum hardware [3, 14, 16–20]. Furthermore, in artificially and carefully designed scenarios, these models have demonstrated rigorous advantages over traditional classical methodologies [12, 21–24].

Both explicit and implicit models have their advantages and limitations. In the training phase, implicit models always achieve lower training errors than explicit models due to a fundamental result known as the representer theorem [25, 26]. However, implicit models can sometimes overfit on the training data, resulting in a decrease in generalization performance [27]. Explicit models can, in certain cases, avoid this overfitting problem [27]. However, explicit models not only have complex training landscapes but also involve additional difficulty in identifying a suitable structure of parameterized quantum

circuits, i.e., ansatz. In addition, certain parameterized quantum circuits are known to encounter a trainability problem, i.e., the barren plateau (BP) issue [28, 29], which refers to exponentially vanishing gradients as the number of qubits used increases.

In the prediction phase, implicit models require the evaluation of quantum kernels $\mathcal{O}(M)$ times, where M is the number of training data points. Assuming that M is on the order of 10^3 – 10^4 , which is commonly applied to kernel methods, and given the current scarcity of access to quantum computing, these factors significantly reduce the applicability of implicit models. In contrast, explicit models only require the execution of a single quantum circuit for making a prediction. In short, there is a trade-off between implicit and explicit models, each with its pros and cons, and there is no framework that allows for the best of both worlds.

In this work, we propose a quantum-classical hybrid algorithm to construct a quantum explicit model that acts as a *surrogate* for a trained quantum implicit model, which we call the explicit quantum surrogate (EQS), as shown in Fig. 1. Our algorithm is composed of two key steps. The first step is the scalable diagonalization of an observable determined by the trained implicit model. An important observation is that predictions made by implicit models can be regarded as the expectation values of observables given as a linear combination of quantum feature states over a training dataset of size M . It is therefore possible to diagonalize the observable with $\text{poly}(M)$ resources, while the dimension of n -qubit quantum feature states is 2^n . Furthermore, we find numerically that such observables are low-rank approximable and that considering $K \ll M$ eigenvectors is sufficient to achieve high prediction accuracy. The second step is the construction of a quantum circuit that approximately diagonalizes the observable. This allows us to evaluate the expectation value by measuring the resulting quantum states in the computational basis. For the construction of the circuit, we use an extended version of the automatic quantum circuit encoding (AQCE) algorithm, origi-

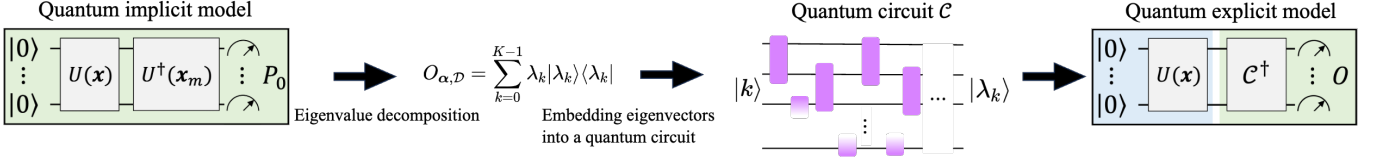


Figure 1. **Overview of the process to convert a trained implicit model to an explicit model (EQS).** An explicit model is constructed from a trained implicit model. First, we find the eigenvalues λ_k and eigenvectors $|\lambda_k\rangle$ of the observable $O_{\alpha, \mathcal{D}}$ in Eq. (3). Utilizing our extended AQCE algorithm, a quantum circuit \mathcal{C} is constructed that satisfies the condition $\mathcal{C}|k\rangle \simeq |\lambda_k\rangle$ for K eigenvectors $\{|\lambda_k\rangle\}_{k=0, \dots, K-1}$ with the accuracy desired by the user, where $|k\rangle$ is the computational basis. This yields an explicit model $\text{Tr}[\rho'(\mathbf{x})O]$, where $\rho'(\mathbf{x}) = \mathcal{C}^\dagger U(\mathbf{x})|\mathbf{0}\rangle\langle\mathbf{0}|U(\mathbf{x})\mathcal{C}$ is a density matrix and $O = \sum_{k=0}^{K-1} \lambda_k |\lambda_k\rangle\langle\lambda_k|$ is an observable.

nally proposed by [30] for constructing a circuit that generates a target state without assuming any fixed ansatz structure. We extend AQCE to generate a circuit for an isometry to diagonalize a low-rank observable. This allows us to construct an explicit model that has a training loss almost equivalent to the trained implicit model. The generated EQS may provide us with insights about ansatz structures suitable for specific datasets. One can also expect to mitigate the BP phenomenon via EQS, as the EQS automatically finds the structure and does not depend on randomly initialized ansatzes, which induce BP.

We evaluate the performance of EQS for classification tasks through numerical simulations. The prediction accuracy of EQS using the MNISQ dataset [31] (a 10-qubit quantum circuit dataset with $M = 10,000$ data points) and the VQE-generated dataset [14] (a 12-qubit quantum circuit dataset with $M = 1,800$ data points) decreases by less than 0.010 compared to trained implicit models. It is notable that these results are obtained by only considering $K \leq 10$ eigenvectors. Additionally, we find that, even when the isometry generated by AQCE has a fidelity of only 0.6, the decrease in prediction accuracy remains at the same level. This suggests that we do not need to optimize the circuit carefully, and the computational cost for optimizing the circuit construction step may be smaller than one might expect. Furthermore, we find that the gradients of the EQS obtained by our method are $10^3 - 10^4$ times larger than when initializing with random parameters, suggesting a significant relaxation of BP. From these observations, we believe that our proposal is a valuable tool not only for reducing the prediction cost of implicit models but also for potentially enhancing the trainability of explicit models.

Preliminary.— Let us first define the notations and terms, which are mostly based on those used in Refs. [5, 27]. Let $\rho(\mathbf{x}) = |\psi(\mathbf{x})\rangle\langle\psi(\mathbf{x})| = U(\mathbf{x})|\mathbf{0}\rangle\langle\mathbf{0}|U^\dagger(\mathbf{x})$ be an n -qubit quantum feature state that encodes an input \mathbf{x} generated via a feature-encoding quantum circuit $U(\mathbf{x})$. We define the explicit model as:

$$f_{\text{explicit}}(\mathbf{x}; \boldsymbol{\theta}) = \text{Tr}[\rho(\mathbf{x})V(\boldsymbol{\theta})^\dagger O V(\boldsymbol{\theta})], \quad (1)$$

where O is an efficiently measurable operator and $V(\boldsymbol{\theta})$ is a parameterized quantum circuit with trainable parameters $\boldsymbol{\theta}$. The training of explicit models is performed by optimizing the parameters $\boldsymbol{\theta}$ to minimize empirical loss. The implicit models

are defined as:

$$f_{\text{implicit}}(\mathbf{x}; \boldsymbol{\alpha}) = \sum_{m=1}^M \alpha_m \text{Tr}[\rho(\mathbf{x}_m)\rho(\mathbf{x})] \quad (2)$$

where $\{\mathbf{x}_m\} =: \mathcal{D}$ is the training dataset, and $\boldsymbol{\alpha} \in \mathbb{R}^M$ is the model parameter which is determined through training. An important observation that we make use of in this work is that f_{implicit} can be rewritten in the form of $f_{\text{implicit}}(\mathbf{x}; \boldsymbol{\alpha}) = \text{Tr}[O_{\alpha, \mathcal{D}}\rho(\mathbf{x})]$ by defining

$$O_{\alpha, \mathcal{D}} = \sum_{m=1}^M \alpha_m \rho(\mathbf{x}_m). \quad (3)$$

Algorithm to construct explicit quantum surrogate.— Our algorithm consists of two main components. The first component is the eigenvalue decomposition of the observable $O_{\alpha, \mathcal{D}}$ of the trained implicit model. The second component is constructing a quantum circuit that produces these eigenvectors. Although there are many ways of achieving this, our choice is to employ the AQCE [30] extended for constructing isometry that allows us to generate circuit without assuming fixed ansatz. The overview of our proposed algorithm is shown in Fig. 1. We describe each component in the sequence below.

First, we perform training of the implicit model and diagonalize the observable $O_{\alpha, \mathcal{D}}$. As $\mathcal{S} = \text{span}\{|\psi(\mathbf{x}_m)\rangle\}$ is an invariant subspace of $O_{\alpha, \mathcal{D}}$, it is sufficient to diagonalize $O_{\alpha, \mathcal{D}}$ within this subspace. For example, we can employ the following process to achieve this. We first determine the set of orthogonal basis vectors $\{|e_i\rangle\}_{i=1}^{\dim(\mathcal{S})}$ of \mathcal{S} using e.g. the Gram-Schmidt process. The inner products $\langle\psi(\mathbf{x}_m)|\psi(\mathbf{x}_{m'})\rangle$ required in the process can be obtained using the Hadamard test [32]. Next, we compute the matrix elements of $O_{\alpha, \mathcal{D}}$ with respect to the new basis $\{|e_i\rangle\}$. They can be calculated as

$$[O_{\alpha, \mathcal{D}}]_{ij} := \langle e_i | O_{\alpha, \mathcal{D}} | e_j \rangle = \sum_{m=1}^M \alpha_m \langle e_i | \rho(\mathbf{x}_m) | e_j \rangle. \quad (4)$$

We can then diagonalize it classically to obtain its eigenvalues $\{\lambda_k\}_{k=0}^{\dim(\mathcal{S})-1}$ and corresponding eigenvectors $\{|\lambda_i\rangle\}_{k=0}^{\dim(\mathcal{S})-1}$ expressed as linear combinations of $|\psi(\mathbf{x}_m)\rangle$. Using these, the implicit model can now be rewritten as $f_{\text{implicit}}(\mathbf{x}; \boldsymbol{\alpha}) = \sum_{k=0}^{\dim(\mathcal{S})-1} \lambda_k \langle \lambda_k | \rho(\mathbf{x}) | \lambda_k \rangle$. Note that it is often possible to

truncate the sum at $K \ll M$ without significant performance decrease, as we will discuss later and show in the numerical experiments. Truncation retains important information in a model while reducing its complexity. It may offer advantages in mitigating overfitting, but we leave such an analysis as future work.

Next, we construct a quantum circuit \mathcal{C} that satisfies $\mathcal{C}|k\rangle \approx |\lambda_k\rangle$ for $k = 0, \dots, K - 1$, where $|k\rangle$ denotes the computational basis states. For this purpose, we extend AQCE [30] to isometries. The original AQCE is an algorithm that generates a circuit that outputs a target state $|\Psi\rangle$ with the desired accuracy. It constructs quantum circuits by iteratively adding two-qubit unitary gates without assuming any fixed ansatz. The optimization is performed in a manner similar to those in tensor network methods [33]. A brief review of AQCE and the extensions done in this work are given in Appendix A and B, respectively. The implicit model can now be translated into an explicit model, that is, an EQS:

$$f_{\text{EQS}}(\mathbf{x}) = \text{Tr}[O\mathcal{C}^\dagger\rho(\mathbf{x})\mathcal{C}] \simeq f_{\text{implicit}}(\mathbf{x}; \boldsymbol{\alpha}), \quad (5)$$

where $O = \sum_{k=0}^{K-1} \lambda_k |k\rangle\langle k|$. It should be noted that the above process of generating EQS can be understood as quantum architecture search (QAS) for finding a well-performing circuit for explicit models [34]. We present an example of the quantum circuit structure found in our numerical simulations, described later in Appendix S4. The analysis of the quantum circuit structure found by EQS is an interesting direction to explore, but it is beyond the scope of this work and will be considered in future research.

The possibility of low-rank approximation significantly affects cost of the AQCE step. Even though it does not raise intrinsic exponential cost to the number of qubits within the iterations for circuit optimization, we would expect that the AQCE would become increasingly difficult when the number of vectors to be constructed, K , is large. The low-rankness can be guaranteed when $\dim(S)$ is small, which we argue here to be expected for quantum features $|\psi(\mathbf{x})\rangle$ that are well-designed, in the sense that “similar” \mathbf{x} are mapped to similar feature vectors $|\psi(\mathbf{x})\rangle$. For supervised learning with input \mathbf{x} and output y , we say data \mathbf{x} and \mathbf{x}' are similar when corresponding y 's are equal or close. For such well-designed features, we can expect that a large portion of $\{|\psi(\mathbf{x}_m)\rangle\}$ is linearly dependent, thus making $\dim(S)$ small. Such well-designedness also guarantees prediction performance. Ref. [22] (Eq. (8)) shows that, if we wish to predict y in the form of $y = \text{Tr}[A\rho(\mathbf{x})]$ for an unknown observable A having a sufficiently small norm, $\text{Tr}(A^2)$, we can achieve a prediction error of $\mathcal{O}(\dim(S))$. We therefore assume that for a well-designed feature that predicts well, the observable of the trained implicit model, $O_{\alpha, \mathcal{D}}$, admits a low-rank approximation.

Numerical analysis of EQS performance.— To evaluate our algorithm, we derive EQS from the implicit model of the support vector machine (SVM) [35, 36] using quantum kernel [3, 4]. We then compare the classification accuracies using two datasets: the MNISQ dataset, [31], which contains 10,000 samples with 10 labels, and the VQE-generated dataset [14], which

contains 1,800 samples with 6 labels. The MNISQ dataset is derived from the quantum encoding of the MNIST dataset [37] and consists of labeled quantum circuits with 10 qubits. The VQE-generated dataset, created using the VQE algorithm [38, 39], comprises labeled quantum circuits with 12 qubits and has the property that output states of circuits with different labels exhibit extremely low fidelity. They are provided in QASM format [40]. Circuits in these datasets are essentially labeled according to the similarity of the output states; those with the same label output similar quantum states. The QASM string is an input data \mathbf{x} in this case, and we simply choose $U(\mathbf{x})$ as the circuit described by the string \mathbf{x} .

To assess how low-rank approximations affect classification accuracy, we compare multiple EQSs, each with a different value of K . In addition, to evaluate how approximations arising within the use of our extended AQCE algorithm for generating isometries affect classification accuracy, we compare two different models. The first model is an EQS represented by Eq. (5) optimized by our algorithm until it satisfies $F^{(k)} := |\langle k|\mathcal{C}^\dagger|\lambda_k\rangle| > 0.6$ for all k . The second model, which we call the exact low-rank model, directly uses the results of low-rank approximations of $O_{\alpha, \mathcal{D}}$, thus avoiding the error induced by the AQCE step. We adopt the one-vs-rest strategy for multi-class classification; that is, we construct a multi-class classifier by combining multiple binary classifiers. Note that this requires us to construct $O_{\alpha, \mathcal{D}}$ and the corresponding circuit \mathcal{C} defining EQS for each label l , which we denote by $O_{\alpha, \mathcal{D}}^{(l)}$ and $\mathcal{C}^{(l)}$. The accuracy shown in the results is defined as the number of correct classifications divided by the total number of test data points. The quantum circuit simulation is performed using Qulacs 0.5.6 [41] in a noiseless environment. We detail the experimental conditions in Appendix C and show the results in Fig. 2. The results for other datasets can be found in Appendix D, which are consistent with the results presented here.

First, we discuss the behavior of the exact low-rank models. In Fig. 2 (a) and (b), we observe that their accuracy improves and approaches the accuracy of the original one as K increases. For instance, with the MNISQ-MNIST dataset as shown in Fig. 2 (a), the exact low-rank model exhibits only a 0.010 decrease in accuracy compared to the implicit model at $K = 10$. For the VQE-generated dataset in Fig. 2 (b), there is a mere 0.014 decrease in accuracy compared to the implicit model at $K = 1$. This can be explained by the fact that $|\psi(\mathbf{x})\rangle$ with different labels exhibit extremely low fidelity in this dataset. Therefore, looking at the fidelity between a state $|\psi(\mathbf{x})\rangle$ for an unknown \mathbf{x} and an average of $|\psi(\mathbf{x}_m)\rangle$ within the same label l in a training set would be sufficient to classify \mathbf{x} . Indeed, the first eigenvector of $O_{\alpha, \mathcal{D}}^{(l)}$ has a high fidelity of over 0.7 with $|\psi(\mathbf{x})\rangle$ belonging to the same label l for most l 's, as shown in Fig. S3 (a) of Appendix E.

Overall, results indicate that high accuracy can be achieved with $K \ll M$ and that low-rank approximation is effective, as M is on the order of $10^3 - 10^4$ for each dataset. Low-rankness can also be seen from the mean value of the cumula-

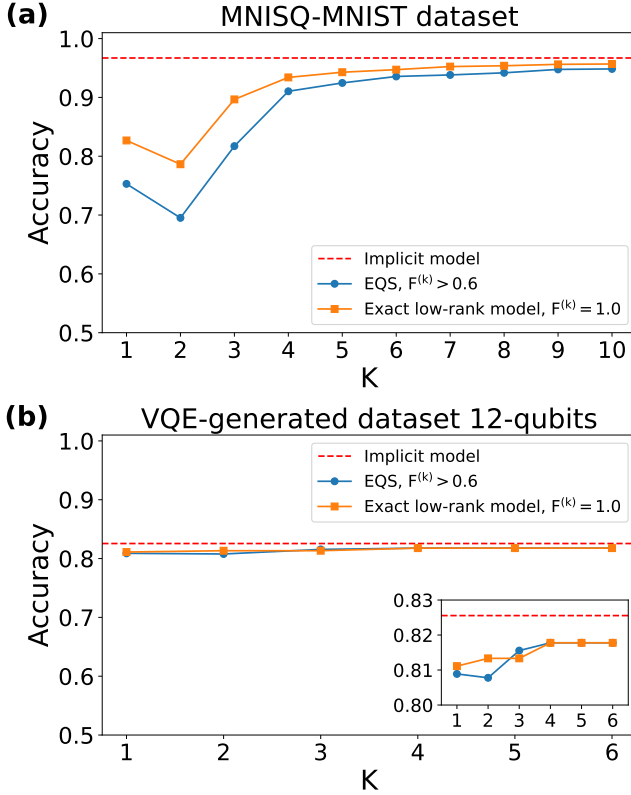


Figure 2. **Performance of EQS on MNISQ-MNIST and 12-qubit VQE-generated dataset.** The vertical axis represents the classification accuracy on the test data. The horizontal axis represents the number of eigenvectors K used in the eigenvalue decomposition of $O_{\alpha, \mathcal{D}}$. The EQS refers to Eq. (5) with fidelities $F^{(k)} > 0.6$ for all k . The exact low-rank model is obtained by exact low-rank approximations of $O_{\alpha, \mathcal{D}}$, which is equivalent to Eq. (5) with $F^{(k)} = 1.0$ for all k . An inset in Fig. 2 (b) provides a detailed, magnified view of a specific area depicted in this panel.

tive contribution ratio $\frac{\sum_{i=0}^{K-1} \lambda_i^2}{\sum_{i=0}^{M-1} \lambda_i^2}$, which is shown in Fig. S3 (b) of Appendix E. For the MNISQ-MNIST and VQE-generated datasets, the values are 0.798 at $K = 10$ and 0.744 at $K = 6$, respectively. We believe that such low-rank natures are reasonable because observables are constructed from linear combinations of the quantum features that encode training data, and the quantum features in this example are well-designed in a sense that data with the same label are mapped to similar quantum states.

Next, we discuss the performance of the EQS models. Fig. 2 (a) and (b) show that the impact of approximations made in the AQCE step on accuracy is surprisingly small. The decrease in accuracy from the exact low-rank model is only 0.008 for the MNIST dataset at $K = 10$. No decrease is observed for the VQE-generated dataset at $K = 6$. It should be emphasized that the condition imposed on fidelities is only $F^{(k)} > 0.6$. We assume this is because the use of imperfect replication of the eigenvectors could change the decision boundaries established in the training phase but did not affect the prediction results due

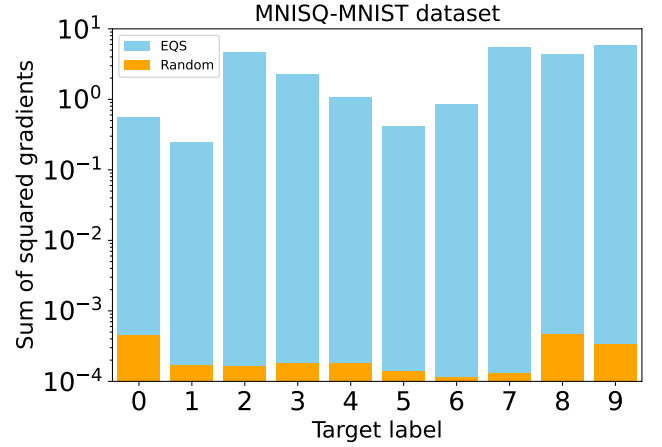


Figure 3. **The sum of squared gradients obtained by explicit models with EQS-initialized ansatz and randomly initialized ansatz.** The vertical axis represents the sum of squared gradients at the first training step. The horizontal axis represents the target label classified by the explicit model.

to the margin preserved by the SVM. Given that the currently available quantum computers are affected by a non-negligible amount of noise, the fact that low target fidelity results in minimal degradation of accuracy may offer an advantage when executing our method on actual devices.

EQS as initialization strategy.— Our strategy to construct the EQS via AQCE automatically finds a circuit \mathcal{C} that defines a well-performing explicit model. It is, therefore, natural to use the circuit found by our algorithm as an initial point for training an explicit model. However, it is not clear if this strategy provides a trainable initialization, that is, non-vanishing gradients. Here, we compare the gradients of the cross-entropy loss function when the explicit models are randomly initialized and when they are initialized to an EQS. To this end, we first construct the EQS in the same manner as in the previous numerical analysis using 10,000 samples from the MNISQ dataset [31] and then compute the gradient of the loss with respect to another 5,000 samples. The gradients are computed by regarding the two-qubit unitary gates in $\mathcal{C}^{(l)}$ as parameterized arbitrary two-qubit unitary gates with 15 parameters. We compare the gradients of two circuits for each label. The first one is randomly initialized, where the parameters are set to random values uniformly in $[0, 2\pi)$. The second one has the same parameters as the EQS. The quantum circuit simulation is performed using Qulacs 0.5.6 [41] under a noiseless environment. The details of the experimental conditions are described in Appendix C.

We present the results in Fig. 3, which shows the sum of squared gradients for each setting. We observe that the gradients of the EQS is 10^3 to 10^4 times larger than that of a randomly initialized ansatz. We believe that this is because when the ansatz is initialized with random parameters, the quantum circuit falls approximately into the unitary 2-design, leading to the BP [28, 29]. It should be stressed that this result

is obtained even though we use the structure found by the AQCE, which has the potential to construct the EQS, but with random parameters. This suggests that the circuit structure itself is not sufficient to avoid BP, but the choice of initial parameters is also a very important component to do so. Using EQS as the initial starting point for training explicit models may mitigate trainability issues.

Conclusion.— In this study, we propose a quantum-classical hybrid algorithm that systematically transforms trained implicit models into explicit ones, which we refer to as EQS. The EQS requires only $\mathcal{O}(1)$ executions of quantum circuits while the implicit model requires $\mathcal{O}(M)$ executions. This is made possible by performing the diagonalization of the implicit model’s observable and finding a circuit for embedding the resulting eigenvectors via an extended version of AQCE. The EQS demonstrated prediction accuracy comparable to that of the implicit model in the classification task utilizing the MNIST dataset [31] and the VQE-generated dataset [14]. The EQS also demonstrated that explicit models with an ansatz initialized with EQS have a sum of squared gradients in the first training step that is 10^3 to 10^4 times larger compared to those with a randomly initialized ansatz.

Future research directions are intriguing and include the following. First, it is interesting to investigate whether the explicit model with an ansatz initialized with EQS can effectively mitigate the overfitting of the implicit model through additional training with new data and improve generalization performance. Another fascinating direction is further training of the EQS as an explicit model, possibly with additional data that could not be handled by an implicit model. Finally, understanding the quantum circuit structure of the EQS, particularly which structure minimizes the cost function for a specific dataset, is an intriguing future issue.

K.M. is supported by JST PRESTO Grant No. JPMJPR2019 and JSPS KAKENHI Grant No. 23H03819. H.U. is supported by JSPS KAKENHI Grant No. JP21H04446, JP21H05182, JP21H05191, and the COE research grant in computational science from Hyogo Prefecture and Kobe City through Foundation for Computational Science. K.F. is supported by JST ERATO Grant No. JPMJER1601 and JST CREST Grant No. JPMJCR1673. This work is supported by MEXT Quantum Leap Flagship Program (MEXTQLEAP) Grant No. JPMXS0118067394 and JPMXS0120319794. We also acknowledge support from the JST COI-NEXT program No. JPMJPF2014.

* u090313j@ecs.osaka-u.ac.jp

† u748119d@ecs.osaka-u.ac.jp

‡ mitarai.kosuke.es@osaka-u.ac.jp

§ ueda.hiroshi.qiqb@osaka-u.ac.jp

¶ fujii@qc.ee.es.osaka-u.ac.jp

- [1] J. Biamonte, P. Wittek, N. Pancotti, P. Rebentrost, N. Wiebe, and S. Lloyd, *Nature* **549**, 195 (2017).
 [2] M. Cerezo, G. Verdon, H.-Y. Huang, L. Cincio, and P. J. Coles,

Nature computational science **2**, 567 (2022).

- [3] V. Havlíček, A. D. Córcoles, K. Temme, A. W. Harrow, A. Kandala, J. M. Chow, and J. M. Gambetta, *Nature* **567**, 209 (2019).
 [4] M. Schuld and N. Killoran, *Physical review letters* **122**, 040504 (2019).
 [5] M. Schuld, *Supervised quantum machine learning models are kernel methods* (2021), arXiv:2101.11020 [quant-ph].
 [6] M. Benedetti, E. Lloyd, S. Sack, and M. Fiorentini, *Quantum Science and Technology* **4**, 043001 (2019).
 [7] M. Cerezo, A. Arrasmith, R. Babbush, S. C. Benjamin, S. Endo, K. Fujii, J. R. McClean, K. Mitarai, X. Yuan, L. Cincio, and P. J. Coles, *Nature Reviews Physics* **3**, 625 (2021).
 [8] K. Bharti, A. Cervera-Lierta, T. H. Kyaw, T. Haug, S. Alperin-Lea, A. Anand, M. Degroote, H. Heimonen, J. S. Kottmann, T. Menke, W.-K. Mok, S. Sim, L.-C. Kwek, and A. Aspuru-Guzik, *Reviews of modern physics* **94**, 015004 (2022).
 [9] K. Mitarai, M. Negoro, M. Kitagawa, and K. Fujii, *Physical review. A* **98**, 032309 (2018).
 [10] M. Schuld, A. Bocharov, K. M. Svore, and N. Wiebe, *Physical review. A* **101**, 032308 (2020).
 [11] J.-G. Liu and L. Wang, *Physical review. A* **98**, 062324 (2018).
 [12] S. Jerbi, C. Gyurik, S. C. Marshall, H. J. Briegel, and V. Dunjko, *Parametrized quantum policies for reinforcement learning* (2021), arXiv:2103.05577 [quant-ph].
 [13] A. Skolik, S. Jerbi, and V. Dunjko, *Quantum* **6**, 720 (2022).
 [14] A. Nakayama, K. Mitarai, L. Placidi, T. Sugimoto, and K. Fujii, *VQE-generated quantum circuit dataset for machine learning* (2023), arXiv:2302.09751 [quant-ph].
 [15] T. Shiota, K. Ishihara, and W. Mizukami, *Digital Discovery* , (2024).
 [16] D. Zhu, N. M. Linke, M. Benedetti, K. A. Landsman, N. H. Nguyen, C. H. Alderete, A. Perdomo-Ortiz, N. Korda, A. Garfoot, C. Breckue, L. Egan, O. Perdomo, and C. Monroe, *Science advances* **5**, eaaw9918 (2019).
 [17] E. Peters, J. Caldeira, A. Ho, S. Leichenauer, M. Mohseni, H. Neven, P. Spentzouris, D. Strain, and G. N. Perdue, *npj Quantum Information* **7**, 1 (2021).
 [18] T. Haug, C. N. Self, and M. S. Kim, *Machine Learning: Science and Technology* **4**, 015005 (2023).
 [19] T. Kusumoto, K. Mitarai, K. Fujii, M. Kitagawa, and M. Negoro, *npj Quantum Information* **7**, 1 (2021).
 [20] K. Bartkiewicz, C. Gneiting, A. Černoč, K. Jiráková, K. Lemr, and F. Nori, *Scientific reports* **10**, 12356 (2020).
 [21] Y. Liu, S. Arunachalam, and K. Temme, *Nature physics* **17**, 1013 (2021).
 [22] H.-Y. Huang, M. Broughton, M. Mohseni, R. Babbush, S. Boixo, H. Neven, and J. R. McClean, *Nature communications* **12**, 2631 (2021).
 [23] N. Pirnay, R. Sweke, J. Eisert, and J.-P. Seifert, *A super-polynomial quantum-classical separation for density modelling* (2022), arXiv:2210.14936 [quant-ph].
 [24] V. Dunjko, Y.-K. Liu, X. Wu, and J. M. Taylor, *Exponential improvements for quantum-accessible reinforcement learning* (2017), arXiv:1710.11160 [quant-ph].
 [25] A. J. Smola, B. Schölkopf, and K. R. Müller, *Neural networks: the official journal of the International Neural Network Society* **11**, 637 (1998).
 [26] B. Schölkopf and A. J. Smola, *Learning with Kernels: Support Vector Machines, Regularization, Optimization, and Beyond* (MIT Press, 2002).
 [27] S. Jerbi, L. J. Fiderer, H. Poulsen Nautrup, J. M. Kübler, H. J. Briegel, and V. Dunjko, *Nature communications* **14**, 517 (2023).
 [28] J. R. McClean, S. Boixo, V. N. Smelyanskiy, R. Babbush, and H. Neven, *Nature communications* **9**, 4812 (2018).

- [29] M. Cerezo, A. Sone, T. Volkoff, L. Cincio, and P. J. Coles, *Nature communications* **12**, 1791 (2021).
- [30] T. Shirakawa, H. Ueda, and S. Yunoki, *Automatic quantum circuit encoding of a given arbitrary quantum state* (2021), arXiv:2112.14524 [quant-ph].
- [31] L. Placidi, R. Hataya, T. Mori, K. Aoyama, H. Morisaki, K. Mitarai, and K. Fujii, *MNISQ: A Large-Scale quantum circuit dataset for machine learning on/for quantum computers in the NISQ era* (2023), arXiv:2306.16627 [quant-ph].
- [32] M. Schuld and F. Petruccione, *Supervised Learning with Quantum Computers* (Springer, 2018).
- [33] G. Evenbly and G. Vidal, *Physical review. B, Condensed matter* **79**, 144108 (2009).
- [34] S.-X. Zhang, C.-Y. Hsieh, S. Zhang, and H. Yao, *Differentiable quantum architecture search* (2020), arXiv:2010.08561 [quant-ph].
- [35] J. Platt, *Adv. Large Margin Classif.* **10** (2000).
- [36] T. Wu, C.-J. Lin, and R. C. Weng, *Journal of machine learning research: JMLR* **5**, 975 (2003).
- [37] Y. Lecun, L. Bottou, Y. Bengio, and P. Haffner, *Proceedings of the IEEE* **86**, 2278 (1998).
- [38] A. Peruzzo, J. McClean, P. Shadbolt, M.-H. Yung, X.-Q. Zhou, P. J. Love, A. Aspuru-Guzik, and J. L. O'Brien, *Nature communications* **5**, 4213 (2014).
- [39] J. Tilly, H. Chen, S. Cao, D. Picozzi, K. Setia, Y. Li, E. Grant, L. Wossnig, I. Rungger, G. H. Booth, and J. Tennyson, *Physics reports* **986**, 1 (2022).
- [40] A. Cross, A. Javadi-Abhari, T. Alexander, N. De Beaudrap, L. S. Bishop, S. Heide, C. A. Ryan, P. Sivarajah, J. Smolin, J. M. Gambetta, and B. R. Johnson, *ACM Transactions on Quantum Computing* **3**, 1 (2022).
- [41] Y. Suzuki, Y. Kawase, Y. Masumura, Y. Hiraga, M. Nakadai, J. Chen, K. M. Nakanishi, K. Mitarai, R. Imai, S. Tamiya, T. Yamamoto, T. Yan, T. Kawakubo, Y. O. Nakagawa, Y. Ibe, Y. Zhang, H. Yamashita, H. Yoshimura, A. Hayashi, and K. Fujii, *Quantum* **5**, 559 (2021).
- [42] F. Pedregosa, G. Varoquaux, A. Gramfort, V. Michel, B. Thirion, O. Grisel, M. Blondel, P. Prettenhofer, R. Weiss, V. Dubourg, J. Vanderplas, A. Passos, D. Cournapeau, M. Brucher, M. Perrot, and E. Duchesnay, *Journal of Machine Learning Research* **12**, 2825 (2011).
- [43] J. Bradbury, R. Frostig, P. Hawkins, M. J. Johnson, C. Leary, D. Maclaurin, G. Necula, A. Paszke, J. VanderPlas, S. Wanderman-Milne, and Q. Zhang, *JAX: composable transformations of Python+NumPy programs* (2018).
- [44] DeepMind, I. Babuschkin, K. Baumli, A. Bell, S. Bhupatiraju, J. Bruce, P. Buchlovsky, D. Budden, T. Cai, A. Clark, I. Danihelka, A. Dedieu, C. Fantacci, J. Godwin, C. Jones, R. Hemsley, T. Hennigan, M. Hessel, S. Hou, S. Kapturowski, T. Keck, I. Kemaev, M. King, M. Kunesch, L. Martens, H. Merzic, V. Mikulik, T. Norman, G. Papamakarios, J. Quan, R. Ring, F. Ruiz, A. Sanchez, L. Sartran, R. Schneider, E. Sezener, S. Spencer, S. Srinivasan, M. Stanojević, W. Stokowiec, L. Wang, G. Zhou, and F. Viola, *The DeepMind JAX Ecosystem* (2020).

Supplemental Material for “Explicit Quantum Surrogates for Quantum Kernel Methods”

Appendix A: Automatic Quantum Circuit Encoding

In this section, we briefly summarize the automatic quantum circuit encoding algorithm (AQCE) [30]. AQCE is an algorithm that produces a quantum circuit \mathcal{C} , which outputs a quantum state $\mathcal{C}|0\rangle$ equivalent to a given arbitrary quantum state $|\Psi\rangle$ with the accuracy desired by the user. AQCE sequentially updates the unitary gates that construct \mathcal{C} using a gradient-free method to maximize the fidelity function $F = \left| \langle 0 | \hat{\mathcal{C}}^\dagger | \Psi \rangle \right|$.

Below, we describe the AQCE algorithm in detail. Assuming that the quantum circuit \mathcal{C} is composed of J two-qubit unitary gates \mathcal{U}_m with $1 \leq m \leq J$, namely,

$$\mathcal{C} = \prod_{m=1}^J \mathcal{U}_m = \mathcal{U}_1 \mathcal{U}_2 \dots \mathcal{U}_J. \quad (\text{A1})$$

When considering an update for the m th unitary gate \mathcal{U}_m , it is convenient to define a fidelity function,

$$F_m = \left| \text{Tr} [|\Psi_{m+1}\rangle \langle \Phi_{m-1}| \mathcal{U}_m^\dagger] \right| \quad (\text{A2})$$

that explicitly focuses only on the degrees of freedom of \mathcal{U}_m , where $|\Psi_m\rangle$ and $\langle \Phi_m|$ are defined by

$$|\Psi_m\rangle = \prod_{j=m}^J \mathcal{U}_j^\dagger |\Psi\rangle = \mathcal{U}_m^\dagger \mathcal{U}_{m+1}^\dagger \dots \mathcal{U}_J^\dagger |\Psi\rangle, \quad (\text{A3})$$

$$\langle \Phi_m| = \langle 0| \prod_{j=1}^m \mathcal{U}_j^\dagger = \langle 0| \mathcal{U}_1^\dagger \mathcal{U}_2^\dagger \dots \mathcal{U}_m^\dagger. \quad (\text{A4})$$

If \mathbb{I}_m denotes the set of indices $\{i, j\}$ corresponding to the qubits on which the unitary gate \mathcal{U}_m acts, then F_m can be rewritten as

$$F_m = \left| \text{Tr}_{\mathbb{I}_m} [\mathcal{F}_m \mathcal{U}_m^\dagger] \right|, \quad (\text{A5})$$

where \mathcal{F}_m is referred to as the fidelity tensor operator and is defined by the equation

$$\mathcal{F}_m = \text{Tr}_{\bar{\mathbb{I}}_m} [|\Psi_{m+1}\rangle \langle \Phi_{m-1}|]. \quad (\text{A6})$$

Here, $\bar{\mathbb{I}}_m$ is the complement of the subsystem \mathbb{I}_m in the total qubit system. If we represent the fidelity tensor operator \mathcal{F}_m and the unitary gate \mathcal{U}_m in matrix form as \mathbf{F}_m and \mathbf{U}_m , respectively, the expression is given by

$$F_m = \left| \text{Tr} [\mathbf{F}_m \mathbf{U}_m] \right|. \quad (\text{A7})$$

The AQCE algorithm updates the unitary gates \mathcal{U}_m to maximize the fidelity function F_m . This can be achieved through singular value decomposition of \mathbf{F}_m , expressed as $\mathbf{F}_m = \mathbf{X} \mathbf{D} \mathbf{Y}$, where \mathbf{X} and \mathbf{Y} are unitary matrices, and \mathbf{D} is a diagonal matrix with non-negative diagonal elements d_n . The fidelity function F_m is then given by

$$F_m = \left| \text{Tr} [\mathbf{X} \mathbf{D} \mathbf{Y} \mathbf{U}_m^\dagger] \right| \quad (\text{A8})$$

$$= \left| \text{Tr} [\mathbf{D} \mathbf{Z}] \right| \quad (\text{A9})$$

$$= \left| \sum_{n=0}^3 d_n [\mathbf{Z}]_{nn} \right| \quad (\text{A10})$$

$$\leq \sum_{n=0}^3 d_n |[\mathbf{Z}]_{nn}|, \quad (\text{A11})$$

where we defined a unitary matrix $\mathbf{Z} = \mathbf{Y} \mathbf{U}_m^\dagger \mathbf{X}$. From this, \mathbf{Z} , which maximizes the fidelity function F_m , satisfies $|[\mathbf{Z}]_{nn'}| = \delta_{nn'}$. Consequently, a unitary gate \mathcal{U}_m that maximizes the fidelity function F_m is given by

$$\mathbf{U}_m = \mathbf{X} \mathbf{Y}. \quad (\text{A12})$$

The pseudocode for the AQCE algorithm is presented in Alg. S1. While the process in line 7 is computationally expensive on classical computers, it can be efficiently computed using a quantum computer with the Hadamard test [30]. In contrast, the calculations from lines 8 to 10 can be efficiently performed on a classical computer.

Algorithm S1 AQCE

Inputs: Quantum state $|\Psi\rangle$, initial number of unitary gates $J_0 \in \mathbb{N}$, increase in the number of unitary gates per sweep $\delta J \in \mathbb{N}$, number of sweep $N \in \mathbb{N}$, maximum number of unitary gates $J_{\max} \in \mathbb{N}$, target fidelity $F_{\text{target}} \in (0, 1]$, set of indices where a two-qubit unitary can be placed \mathbb{B}

Output: Quantum circuit \mathcal{C}

```

1: Initialization:  $\mathcal{C} \leftarrow I$  and  $J \leftarrow J_0$ 
2: while  $J < J_{\max} \wedge F < F_{\text{target}}$  do
3:   Add  $\delta J$  two-qubit gates to  $\mathcal{C}$ 
4:    $J \leftarrow J + \delta J$ 
5:   for counter = 1 to  $N$  do
6:     for  $m = 1$  to  $J$  do
7:       For all indices  $\mathbb{I}_l \in \mathbb{B}$ , find the representation matrix  $\mathbf{F}_{m,l}$  for  $\mathcal{F}_{m,l} = \text{Tr}_{\mathbb{I}_l} [|\Psi_{m+1}\rangle \langle \Phi_{m-1}|]$ .
8:       For all  $\mathbf{F}_{m,l}$ , perform the singular value decomposition  $\mathbf{F}_{m,l} = \mathbf{X}_l \mathbf{D}_l \mathbf{Y}_l$  and compute  $S_l = \sum_{n=0}^3 [\mathbf{D}_l]_{nn}$ 
9:       Find  $l = l^*$  that maximizes  $S_l$ .
10:      Calculate  $\mathbf{U}_m^* = \mathbf{X}_{l^*} \mathbf{Y}_{l^*}$  and determine the unitary gate  $\mathcal{U}_{m,l^*}^*$  that corresponds to  $\mathbf{U}_m^*$  and acts on  $\mathbb{I}_l$ .
11:       $\mathcal{U}_m \leftarrow \mathcal{U}_{m,l^*}^*$ 
12:     end for
13:   end for
14: end while

```

Appendix B: Extending AQCE to isometries

In this section, we detail the extension of AQCE to isometries. More concretely, our extended AQCE is an algorithm designed to generate a quantum circuit \mathcal{C} that satisfies $\mathcal{C}|k\rangle \approx |\Psi^{(k)}\rangle$ for a set of orthogonal quantum states $\{|\Psi^{(k)}\rangle\}_{0 \leq k \leq K-1}$, under the condition that the global phase of quantum states is disregarded. Similar to AQCE, we assume that the quantum circuit is composed of J two-qubit unitary gates, as shown in Eq. (A1). We modify the fidelity functions F and F_m from AQCE as follows:

$$F = \sum_{k=0}^{K-1} F^{(k)} = \sum_{k=0}^{K-1} \left| \langle k | \mathcal{C}^\dagger | \Psi^{(k)} \rangle \right|, \quad (\text{B1})$$

For convenience, we define

$$F_m = \sum_{k=0}^{K-1} \left| \text{Tr} \left[|\Psi_{m+1}^{(k)}\rangle \langle \Phi_{m-1}^{(k)} | \mathcal{U}_m^\dagger \right] \right|, \quad (\text{B2})$$

where

$$|\Psi_m^{(k)}\rangle = \prod_{j=m}^J \mathcal{U}_j^\dagger |\Psi^{(k)}\rangle = \mathcal{U}_m^\dagger \mathcal{U}_{m+1}^\dagger \dots \mathcal{U}_J^\dagger |\Psi^{(k)}\rangle, \quad (\text{B3})$$

$$\langle \Phi_m^{(k)} | = \langle k | \prod_{j=1}^m \mathcal{U}_j^\dagger = \langle k | \mathcal{U}_1^\dagger \mathcal{U}_2^\dagger \dots \mathcal{U}_m^\dagger. \quad (\text{B4})$$

Using \mathbb{I}_m defined in Appendix A, F_m can be rewritten as

$$F_m = \sum_{k=0}^{K-1} \left| \text{Tr}_{\mathbb{I}_m} \left[\mathcal{F}_m^{(k)} \mathcal{U}_m^\dagger \right] \right|. \quad (\text{B5})$$

Here, $\mathcal{F}_m^{(k)}$ is defined as:

$$\mathcal{F}_m^{(k)} = \text{Tr}_{\mathbb{I}_m} \left[|\Psi_{m+1}^{(k)}\rangle \langle \Phi_{m-1}^{(k)} | \right]. \quad (\text{B6})$$

If we represent the fidelity tensor operator $\mathcal{F}_m^{(k)}$ and the unitary gate \mathcal{U}_m as matrices $\mathbf{F}_m^{(k)}$ and \mathbf{U}_m , respectively, we can reformulate the fidelity function F_m as follows:

$$F_m = \sum_{k=0}^{K-1} \left| \text{Tr} \left[\mathbf{F}_m^{(k)} \mathbf{U}_m \right] \right|. \quad (\text{B7})$$

To optimize the unitary gate \mathcal{U}_m to maximize the fidelity function F_m using the AQCE algorithm strategy, we reformulate the fidelity function F_m in the same form as in Eq. (A7). This can be achieved if $\text{Tr} \left[\mathbf{F}_m^{(k)} \mathbf{U}_m \right]$ is always real and positive in all cases. To achieve this, we transform $|\Psi^{(k)}\rangle$ as follows to cancel its global phase:

$$|\Psi^{(k)}\rangle \rightarrow e^{i\theta^{(k)}} |\Psi^{(k)}\rangle, \quad (\text{B8})$$

where $\theta^{(k)} \in [0, 2\pi)$. As a result, F_m can be written as

$$F_m = \sum_{k=0}^{K-1} \left| \text{Tr} \left[e^{i\theta_m^{(k)}} \mathbf{F}_m^{(k)} \mathbf{U}_m \right] \right| = \left| \text{Tr} \left[\mathbf{F}_m \mathbf{U}_m \right] \right|, \quad (\text{B9})$$

where $\mathbf{F}_m = \sum_{k=0}^{K-1} e^{i\theta_m^{(k)}} \mathbf{F}_m^{(k)}$. It should be noted that changes in the global phase of quantum states $|\Psi^{(k)}\rangle$ do not affect the construction of our EQS. This is because low-rank approximations of an observable of implicit models and the fidelity function F_m are invariant with respect to the global phase of quantum states $|\Psi^{(k)}\rangle$. Furthermore, it is worth mentioning that even if some applications require the global phase, simply applying this phase to the initial state before applying the quantum circuit suffices. In this case, we update the unitary gate \mathcal{U}_m following the update of the phase $\theta_m^{(k)}$. The optimization cost of the phase $\theta_m^{(k)}$ is almost negligible compared to the fidelity tensor in Eq. (B6). We present the pseudo-algorithm for the extended AQCE in Alg. S2.

We note that it is possible to update the unitary gate \mathcal{U}_m to maximize the fidelity function using gradient methods, without granting additional degrees of freedom to the phase of the quantum state $|\Psi^{(k)}\rangle$. Specifically, we parameterize the matrix representation of the two-qubit unitary gate \mathcal{U}_m , denoted as \mathbf{U}_m , as $\mathbf{U}_m(\boldsymbol{\theta}_m)$. We then optimize parameters $\boldsymbol{\theta}_m$ to maximize the fidelity function $F_m = \sum_{k=0}^{K-1} \left| \langle \Phi_{m-1}^{(k)} | \mathbf{U}_m^\dagger(\boldsymbol{\theta}_m) | \Psi_{m+1}^{(k)} \rangle \right|$. In this case, we do not need to compute the fidelity tensor operator, although we incur an additional cost in computing the gradient. Therefore, it may be beneficial if the cost of computing the fidelity tensor operator exceeds the cost of computing the gradient. Such situations may arise when using actual quantum computers for execution.

Algorithm S2 Extended AQCE

- 1: **Inputs:** Set of orthogonal quantum states $\{|\Psi^{(k)}\rangle\}_k$, initial number of unitary gates $J_0 \in \mathbb{N}$, increase in the number of unitary gates per sweep $\delta J \in \mathbb{N}$, number of sweep $N \in \mathbb{N}$, maximum number of unitary gates $J_{\max} \in \mathbb{N}$, set of target fidelities $\left\{ F_{\text{target}}^{(k)} \right\}_k$, $F_{\text{target}}^{(k)} \in (0, 1]$ for the quantum state $|\Psi^{(k)}\rangle$, set of indices where a two-qubit unitary can be placed \mathbb{B}
 - 2: **Output:** Quantum Circuit \mathcal{C}
 - 3: Initialization: $\mathcal{C} \leftarrow I$ and $J \leftarrow J_0$
 - 4: **while** $J < J_{\max} \wedge F^{(0)} < F_{\text{target}}^{(0)} \wedge \dots \wedge F^{(K-1)} < F_{\text{target}}^{(K-1)}$ **do**
 - 5: Add δJ two-qubit gates to \mathcal{C}
 - 6: $J \leftarrow J + \delta J$
 - 7: **for** counter = 1 to N **do**
 - 8: **for** $m = 1$ to J **do**
 - 9: For all indices $\mathbb{I}_l \in \mathbb{B}$ and k , find the representation matrix $\mathbf{F}_{m,l}^{(k)}$ for $\mathcal{F}_{m,l}^{(k)} = \text{Tr}_{\bar{\mathbb{I}}_l} \left[\left| \Psi_{m+1}^{(k)} \right\rangle \left\langle \Phi_{m-1}^{(k)} \right| \right]$.
 - 10: For all indices $\mathbb{I}_l \in \mathbb{B}$ and k , find the phase component $\phi_{m,l}^{(k)}$ for $\text{Tr} \left[\mathbf{F}_{m,l}^{(k)} \mathbf{U}_m^\dagger \right]$.
 - 11: $\theta_{m,l}^{(k)} \leftarrow -\phi_{m,l}^{(k)}$ for all l and k
 - 12: Calculate $\mathbf{F}_{m,l} = \sum_{k=0}^{K-1} e^{i\theta_{m,l}^{(k)}} \mathbf{F}_{m,l}^{(k)}$ for all l
 - 13: Execute steps 8-11 in Alg. S1.
 - 14: **end for**
 - 15: **end for**
 - 16: **end while**
-

Appendix C: Detailed conditions of numerical experiments

First, we provide the details of the numerical experiments in Fig. 2. As our implicit model, we employ a kernel support vector machine (SVM) model [35, 36]. We employ the one-vs-rest approach for multi-class classification; that is, we train

a separate SVM model $f_{\text{implicit}}^{(l)}$ for each class l to distinguish it from all other classes. The overall prediction for an input \mathbf{x} is made by outputting $\text{argmax}_l f_{\text{implicit}}^{(l)}(\mathbf{x})$. The SVM model is trained using scikit-learn 1.3.0 [42] with a regularization strength of $C = 1.0$. To construct EQS, we first perform an exact diagonalization of $O_{\alpha, \mathcal{D}}^{(l)}$ to determine its eigenvalues $\lambda^{(l)}$ and eigenvectors $|\lambda^{(l)}\rangle$. Then, we generate quantum circuits $\mathcal{C}^{(l)}$ using Alg. S2. The parameters for the algorithms are set as $F_{\text{target}}^{(0)} = 0.6, \dots, F_{\text{target}}^{(K-1)} = 0.6, J_0 = 12$ and $\delta J = 6$, without specifying J_{max} . We run noiseless quantum circuit simulations using Qulacs 0.5.6 [41]. For the input data, we focus on the MNIST dataset from the MNISQ dataset [31], which has a fidelity of over 95%. We sample 1,000 data points for each label from the dataset, totaling 10,000 data points across all labels. Half of the data from each label is allocated for training, with the remaining half designated for testing. Additionally, we focus on 12-qubit VQE-generated datasets [14]. The datasets comprise six labels. For each label, we use all 300 data points, resulting in a total of 1,800 data points. Half of the data for each label is allocated for training, with the remaining half used for testing.

Next, we provide the details for the numerical experiments in Fig. 3. In these experiments, we focus on the MNISQ-MNIST dataset [31] with fidelity condition 95%. Let $\mathcal{C}^{(l)}(\boldsymbol{\theta})$ be a parameterized quantum circuit obtained by treating the two-qubit unitary gates in $\mathcal{C}^{(l)}$ of EQS as parameterized arbitrary two-qubit unitary gates with 15 independent parameters. The number of parameters is approximately 2,000 to 3,000, depending on the structure found via AQCE. Furthermore, let

$$f^{(l)}(\mathbf{x}; \boldsymbol{\theta}) = \text{Tr}[O^{(l)} \mathcal{C}^{(l)}(\boldsymbol{\theta})^\dagger \rho(\mathbf{x}) \mathcal{C}^{(l)}(\boldsymbol{\theta})], \quad (\text{C1})$$

where $O^{(l)} = \sum_{k=0}^{K-1} \lambda_k^{(l)} |k\rangle\langle k|$, and

$$p^{(l)}(\mathbf{x}; \boldsymbol{\theta}) = \frac{1}{1 + e^{-f^{(l)}(\mathbf{x}_m; \boldsymbol{\theta})}}. \quad (\text{C2})$$

We define the weighted cross-entropy function as the loss on an input dataset \mathcal{X} :

$$L^{(l)}(\boldsymbol{\theta}; \mathcal{X}) = -\frac{1}{M} \sum_{\mathbf{x} \in \mathcal{X}} \left[\frac{M_{\neq l}}{M} y_{\mathbf{x}} \log(p^{(l)}(\mathbf{x}; \boldsymbol{\theta})) + \frac{M_l}{M} (1 - y_{\mathbf{x}}) \log(1 - p^{(l)}(\mathbf{x}; \boldsymbol{\theta})) \right]. \quad (\text{C3})$$

Here, $M = |\mathcal{X}|$, M_l is the number of data points belonging to the label l , and $M_{\neq l}$ is the number of data points belonging to other labels, that is, $M_{\neq l} = \sum_{l' \neq l} M_{l'}$. $y_{\mathbf{x}} \in \{0, 1\}$ is the label corresponding to the input data \mathbf{x} , where data belonging to l are labeled as 1, and all others are labeled as 0. The gradients of the loss function, $\frac{\partial L^{(l)}}{\partial \boldsymbol{\theta}}$, are computed using Qulacs 0.5.6 [41] and JAX 0.4.30 [43]. For \mathcal{X} , we sample $M_l = 500$ data points for each label from the dataset that were not used in the construction of EQS, totaling $M = 5000$ data points across all labels. The quantum circuit simulation is performed under a noiseless environment. Half of the data from each label is used for evaluating the gradients.

Appendix D: Additional numerical experiments

1. Experiments on additional datasets

Here, we present the results for the MNISQ-Fashion MNIST dataset [31] and an 8-qubit VQE-generated dataset [14]. The results are shown in Fig. S1. The simulation conditions are identical to those described in Appendix C. In Fig. S1 (a), we can see that the accuracy of the exact low-rank model improves and approaches the accuracy of the original implicit model as K increases, which is consistent with the results discussed in the main text. For example, the exact low-rank model exhibits only a 0.004 decrease in accuracy when compared to the implicit model at $K = 10$ for the MNISQ-Fashion MNIST dataset. For the VQE-generated dataset in Fig. S1 (b), the accuracy of the exact low-rank model saturates already at $K = 1$. This may be because the accuracy is 0.998 at $K = 1$, sufficiently close to 1.0, leaving no room for improvement in accuracy with the increase of K . The reason for such a high accuracy may be attributed to factors discussed in the main text; in the case of the VQE-generated dataset, the first eigenvector of the observable in the implicit model exhibits high fidelity corresponding to its label.

2. Further training of the EQS

In relation to the numerical experiments in Fig. 3, we attempt further training of explicit models defined in (C1) with the loss function (C3). We optimize the parameters $\boldsymbol{\theta}$ of the ansatz $\mathcal{C}^{(l)}(\boldsymbol{\theta})$ using the Adam optimizer with the following hyperparameters: $\alpha = 0.009$, $\beta_1 = 0.9$, $\beta_2 = 0.999$, $\varepsilon = 10^{-8}$, and $\bar{\varepsilon} = 10^{-8}$. The batch size is set to 1000. The optimization is performed using Qulacs 0.5.6 [41], JAX 0.4.30 [43], and Optax 0.2.3 [44]. The results are shown in Fig. S2. Fig. S2 (a) and (b) show that for some

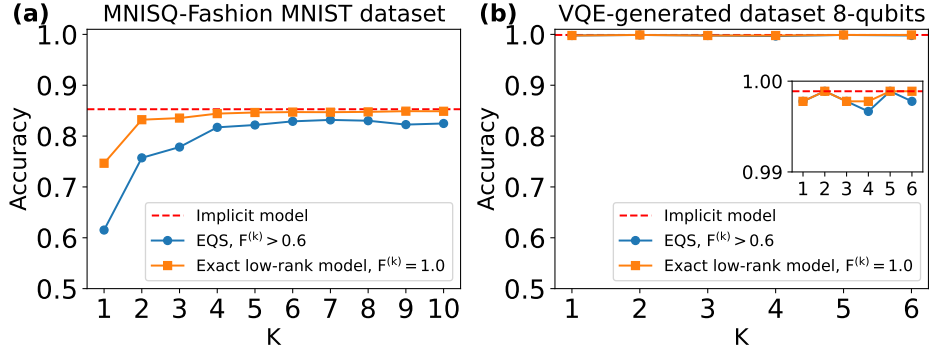


Figure S1. **Performance of EQS on MNISQ-Fashion MNIST and 8-qubit VQE-generated dataset.** Notations follow that of Fig. 2 in the main text.

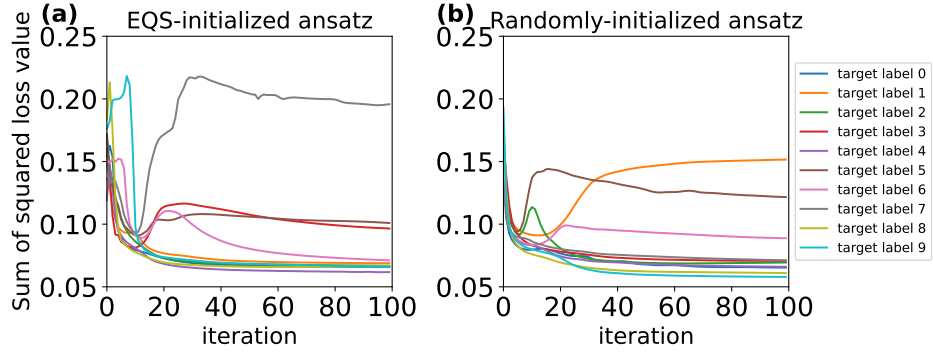


Figure S2. **The sum of squared losses obtained by explicit models with an EQS-initialized ansatz and a randomly-initialized ansatz.** The vertical axis represents the sum of squared loss. The horizontal axis represents the number of iteration steps.

labels, the loss does not converge well to lower values. Through repeated numerical experiments, we found that the convergence is highly dependent on the hyperparameters of the optimization algorithm. We believe that properly setting the hyperparameters of the optimization algorithm could potentially improve the convergence of the loss. The analysis of hyperparameter tuning in the training of explicit models remains a subject for future research.

Appendix E: Additional analysis

In Fig. S3 (a), we show the average fidelity between the first eigenvector of the observable of the implicit model, as discussed in Figs. 2 (b) and S1 (b), and the data belonging to the classes distinguished by this model for each label is shown. In Fig. S3 (b), we present the cumulative contribution ratio $\frac{\sum_{i=0}^{K-1} \lambda_i^2}{\sum_{i=0}^{M-1} \lambda_i^2}$ for the observables of the implicit models discussed in Figs. 2 and S1. In Fig. S4, we show an example of the quantum circuit structure of the EQS trained for label 0 of MNISQ-MNIST dataset.

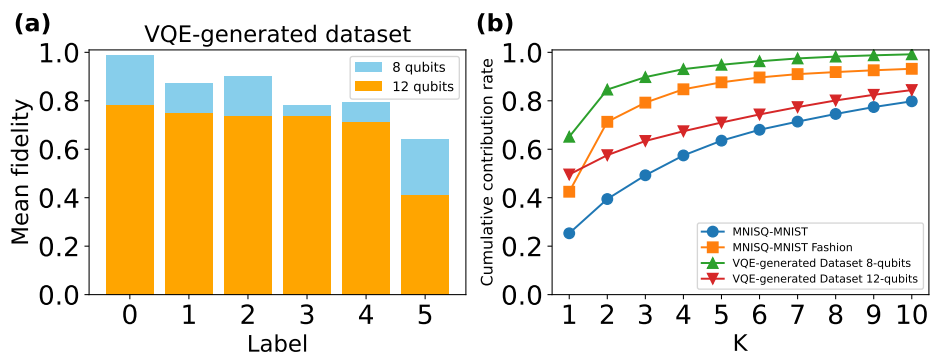


Figure S3. (a) Average fidelity between the first eigenvector of the observables of implicit models and the data for distinguished classes. The vertical axis represents the average fidelity between the first eigenvector of the observables of the implicit model and the data belonging to the classes distinguished by this model. (b) The mean value of the cumulative contribution ratios for the observables of each implicit model.

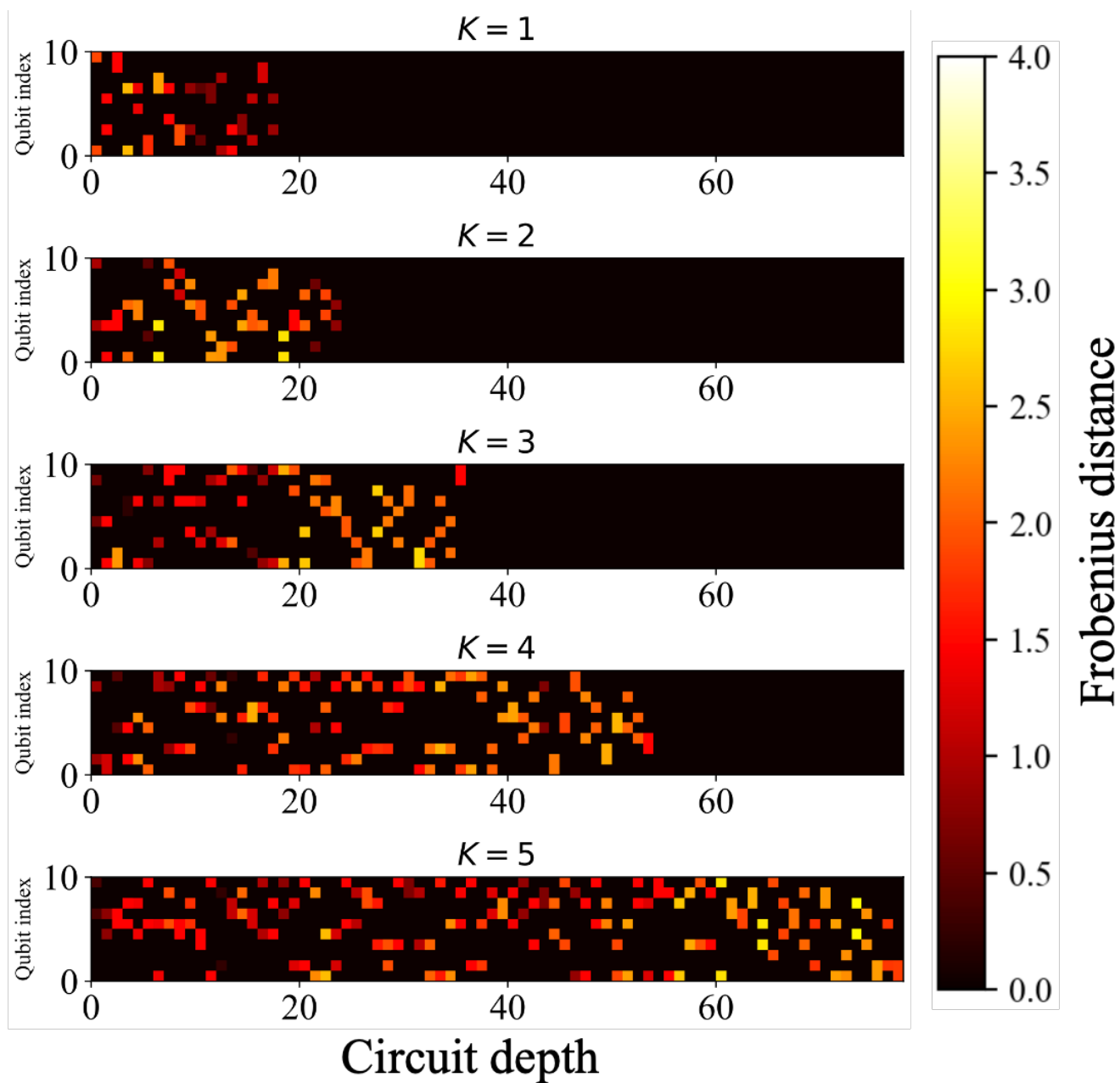


Figure S4. A visualization of the quantum circuit that defines the EQS for MNISQ-MNIST dataset. The vertical axis represents the index numbers of the qubits, while the horizontal axis corresponds to the depth of the quantum circuit. The color represents the Frobenius distance between the unitary gates and the identity matrix.